Journal Pre-proof

Geomechanical modeling of fault-propagation folds: A comparative analysis of finite-element and the trishear kinematic model

Berenice Plotek, Jeremías Likerman, Ernesto Cristallini

PII: S0191-8141(24)00016-6

DOI: https://doi.org/10.1016/j.jsg.2024.105064

Reference: SG 105064

To appear in: *Journal of Structural Geology*

Received Date: 7 July 2023

Revised Date: 6 December 2023

Accepted Date: 13 January 2024

Please cite this article as: Plotek, B., Likerman, Jeremí., Cristallini, E., Geomechanical modeling of fault-propagation folds: A comparative analysis of finite-element and the trishear kinematic model, *Journal of Structural Geology* (2024), doi: https://doi.org/10.1016/j.jsg.2024.105064.

Geomechanical modeling of fault-propagation folds: a comparative analysis of finite-element and the trishear kinematic model

Berenice Plotek[a*]; Jeremías Likerman[a]; Ernesto Cristallini[a]

a Laboratorio de Modelado Geológico (LaMoGe), Instituto de Estudios Andinos "Don Pablo Groeber" (IDEAN), Universidad de Buenos Aires-CONICET. E mail address :berenice@gl.fcen.uba.ar; jlikerman@gl.fcen.uba.ar; ernesto@gl.fcen.uba.ar. Postal Address: Intendente Guiraldes 2160, Ciudad Autónoma de Buenos Aires - C1428EHA, Argentina.

Abstract

Fault-propagation folds are common structures within fold and thrust belts. The trishear kinematic model has been widely used to understand the kinematics and geometry of these folds, effectively reproducing various characteristics. However, the resulting geometry of natural prototypes may diverge from the predictions of the trishear model depending on the rheological properties involved in the deformation. In order to address this limitation, finite element viscoplastic numerical models were implemented. The analysis revealed that in models with a 15° fault angle, these simulations develop a mechanically weaker discontinuity, which is defined as the low viscosity zone (LVZ). The LVZ induces faulting and absorbs slip, causing deviations of velocity vectors from parallel alignment with the main reverse ramp. In models with fault angles set at 25° or 35°, the kinematic vectors of the hanging wall aligned parallel to the ramp, and a zone of progressive rotation of the velocity vectors was observed in the forelimb, resembling the theoretical trishear zone. In these scenarios, the resulting folds exhibited greater symmetry. However, in cover layers with a viscosity equal to 10^{20} Pa s, the forelimb exhibits the highest velocities, which is attributed to material flow toward the footwall.

Keywords:

Finite-element numerical model

Fault-propagation folding

Trishear method

Kinematic field

1. Introduction

Fault-propagation folds are commonly observed structures in fold and thrust belts (Mitra, 1990; Pace et al., 2022). The concept of fault-propagation folding was originally proposed by Suppe and Medwedeff (1984, 1990), who suggested that the fold develops gradually at the fault tip during thrust-fault propagation. The growth of the structure is influenced by variations in slip along the fault. At the fault tip, slip is assumed to be zero, and the decrease in slip is balanced by the folding of the material above the fault (Hardy and Ford, 1997; Mitra and Mount, 1998; Allmendinger, 1998; Brandes and Tanner, 2014). Fault-propagation folds typically exhibit an asymmetric geometry with a steep or even overturned forelimb and a less steep backlimb (Jabbour et al., 2012; Hughes et al., 2014; Grothe et al., 2014; Khalifeh-Soltani et al., 2021). Understanding the temporal evolution of such folds requires a fundamental comprehension of fault-propagation kinematics. Extensive research on fault-propagation folds has been conducted using various methodologies, including analog models (Storti et al., 1997; Mitra and Miller, 2013; Bonanno et al., 2017) and numerical simulation (Cardozo et al., 2003; Hardy and Finch, 2007; Hughes and Shaw, 2015; Meng and Hogetts, 2019; Ju et al., 2023), both of which contribute to the understanding of fold development.

Over the past 25 years, the trishear kinematic model (Erslev, 1991) has been widely used to explain the kinematics and geometry of fault-propagation folds (Allmendinger, 1998; Cristallini and Allmendinger, 2001; Zehnder and Allmendinger, 2002; Allmendinger et al., 2004; Cristallini et at., 2004; Pei et al., 2014; Coleman et al., 2019; Shi and Ling, 2022). The trishear kinematic model describes a triangle-shaped zone of shearing that extends from the fault tip. This model concentrates shear strain within the triangular zone, resulting in translational deformation of particles in the hanging wall while largely fixing them in the footwall. The velocity field is determined by satisfying the condition of area preservation while also being compatible with the velocity conditions at the boundaries of the triangular shear zone (Zehnder and Allmendinger, 2000). The trishear model successfully reproduces various characteristics of fault-propagation folds, including footwall synclines, progressive rotation of the forelimb, variations in bed thickness toward the fault (Hardy and Ford, 1997; Cardozo and Aanonsen, 2009; Hardy and Allmendinger, 2011), and the occurrence of heterogeneous strain patterns (Liu et al., 2012; Grothe et al., 2014; Khalifeh-Soltani et al., 2021). However, challenges exist in describing the primary variables of the trishear model, such as the slip of the hanging block, the propagation-to-slip ratio (P/S), and the apical angle of the trishear zone (Allmendinger, 1998; Hardy, 2019).

Previous studies have shown that the apical angle is a key parameter in the trishear model (Shi and Ling, 2022; Hardy and Finch, 2007). Lower apical angle values are required to reconstruct the structure as the heterogeneity of the sedimentary cover increases (Hardy and Finch, 2007). However, further research is needed to understand how the mechanical characteristics of the materials involved in folding relate to the apical angle. To address this, finite element numerical models were performed to simulate fault-propagation folding and extract the velocity field during the evolution of the structure. In the simulations, visco-plastic rheology was employed for the materials, and the viscosity of the cover layers was varied (ranging from 10^{20} to 10^{22} Pa s), while the basement remained consistent across all the experiments. These models were used to compare the velocity field with the theoretically predicted trishear model.

The goal of this paper is to highlight how the viscosities of the beds influence the kinematic field deviation from the trishear method. Finite element models are analyzed to understand how this property affects the evolution of fault-propagation folds. This is achieved by reproducing the development of a fold above a rigid block affected by a reverse fault with varying dip angles. In this context, this research endeavors to quantitatively evaluate the extent of error introduced when employing the theoretical model to address natural prototypes.

2. Methods

Finite element models were employed to investigate fault-propagation folding in a two-dimensional setting, considering a basement-involved fault with two layers representing a homogeneous cover. The simulations utilized the finite-element particle-in-cell software, Underworld2 (Moresi et al., 2003; 2007; Beucher et al., 2019), which has demonstrated successful application in analyzing lithosphere processes (Gianni et al., 2023; Likerman et al., 2021; Capitanio et al., 2020; Cenki-Tok et al., 2020), contractional structures (Rey et al., 2017), and buckling problems (Smith et al., 2021). Underworld2 combines an Eulerian finite element method with Lagrangian particles integrated within the elements, allowing for effective handling of multiple materials and tracking their properties throughout the model's evolution.

The simulations were based on the equations of conservation of momentum, mass, and energy, assuming incompressibility and utilizing the Boussinesq approximation. To obtain the velocity field during the development of conventional fault-propagation folds (Brandes and Tanner, 2014), a series of finite element simulations were conducted, subjecting a multi-layer sequence to shortening. The resulting geometries and velocity field were analyzed and compared with those predicted by the trishear model. The theoretical trishear kinematic fields were obtained from the Andino 3D software (Cristallini et al., 2021).

2.1. Finite element modeling setup

The model setup is based on natural examples of fault-propagation folds, including the one identified in Sierra Las Peñas-Las Higueras, Mendoza, Argentina (Ahumada et al., 2006), and previous numerical simulations of fault-propagation folding (Plotek et al., 2022). The model has dimensions of 150 kilometers in width and 25 kilometers in height. It consists of two horizontal layers with identical mechanical properties, with a bottom layer representing the basement. The bottom layer has a thickness of 7.5 km, while the two layers above it are each 3.75 km thick (refer to Figure 1). Within the bottom layer, a fault plane with a width of 5 km is introduced at a distance of 40 km from the left wall. The dipping angle of the fault varies between 15° and 35°, depending on the specific model. The fault zone exhibits an internal angle of friction of 10° and a cohesion of 2 MPa (Barton, 2013; Reston, 2020; Treffeisen and Henk, 2020). This plane serves as a pre-existing damage zone and is introduced with the objective of concentrating deformation in that specific area. Once located, the plasticity enables the partial reproduction of the fault's growth. Additionally, a layer with properties resembling air is added on top. This configuration simulates a conventional fault-propagation fold, where folding occurs as the fault steps up over a ramp (Brandes and Tanner, 2014). The fault is characterized by a simple structure, consisting of a ramp segment without bending or branching.

The model design is resolved with a mesh of 128 x 32 cells. All models are run for 1 Myr, and contractional deformation is enforced through velocity boundary conditions, with an imposed velocity of 1.2 cm/yr applied to the left-moving wall. The models have free-slip boundary conditions at the base and top surfaces. The footwall particles are fixed to resemble the original trishear approach proposed by Erslev (1991).

A suite of 12 models is conducted, varying the angle of the reverse fault and the viscosity of the cover. The tested viscosities range from 10^{20} to 10^{22} Pa s. The models utilize uniform viscosity deformation, which is a simplification technique employed in previous numerical studies (e.g., Holt and Condit, 2021). The plasticity parameters, density, viscosity, and cohesion of the materials are specified in Table 1. Densities are considered to be linear with temperature in all the finite element models. The boundary temperatures remain constant throughout the entire model run, with a linear gradient established from 293º K at the surface to 750º K at the bottom of the model.

Insert Figure 1 here.

Insert Table 1 here.

2.2. Kinematic modeling

In order to simulate fault-propagation folds effectively, the trishear model has been widely adopted as a reliable kinematic model. It has been implemented in various software packages (Allmendinger, 1998; Cristallini and Allmendinger, 2001; Cardozo, 2005; Allmendinger et al., 2012; Oakley and Fisher, 2015). In this study, the Andino 3D software was used, which calculates the velocity field based on the equations proposed by Zehnder and Allmendinger (2000). The software generates a grid of points based on user-defined XY coordinates of the bedding points and calculates the velocity field incrementally. The trishear zone is assumed to be symmetric in all cases. The user can input parameters such as P/S (propagation-to-slip ratio), apical angle, total steps, and fault dip to define the kinematic method. By comparing the geometry and kinematics of fault-propagation folds obtained from the trishear method with various mechanical-numerical finite element models, it is possible to assess the influence of viscosity variations and reverse fault dipping angles on the apical angle.

In the analysis of theoretical models, it is generally advisable to start by examining the simplest scenarios when approximating a geometry using a theoretical model like trishear. In this study, a symmetric apical angle was used to approximate the kinematic fields of the finite element models. The primary focus of this work was to investigate the apical angle, which was considered the main parameter of interest. To explore the effects of different apical angles, a series of theoretical trishear models were executed with 5-degree increments. Previous research has indicated that the propagation-to-slip ratio also significantly impacts the geometry of the beds (Allmendinger, 1998; Shi and Ling, 2022). A specific stage in the evolution of the finite element models was selected, where the fault does not propagate excessively across the layers. Consequently, specific P/S values were assumed for the kinematic comparison at this particular stage.

3. Results

The results of the finite element (FE) models are presented in Figure 2 and Figure 3, which depict the viscosity and velocity fields for different fault angles ranging from 15º to 35º, respectively. These plots illustrate two sequential shortening periods at 0.4 and 1.0 Myr.

3.1. Geometrical evolution of the models

3.1.1 Fault angle of 15º

The suite of FE models with a fault angle set at 15º exhibits an asymmetric structure, where the frontal syncline is located to the left of the imposed main reverse fault, rather than aligned with it in the forelimb (Figure 2.a-f). The simulations reveal the presence of a low viscosity zone (LVZ, hereinafter) in addition to the imposed main reverse fault and its associated backthrust. The LVZ, characterized by a viscosity of approximately 10^{21} Pa s, acts as a mechanically weaker discontinuity that induces faulting and accommodates slip. Consequently, the resulting fault displays steeper dip angles compared to the initially induced main fault (Figures 2.b, 2.d, and 2.f). This feature becomes more prominent in cover layers with lower viscosity (Figures 2.b and 2.d). Figure 2.b illustrates that the low viscosity values are concentrated within a 4 km fault (LVZ) developed above the imposed main reverse ramp. In the remaining FE models of the suite, the low viscosity values form a zone of varying width (LVZ) from the early stages of the model's evolution (Figures 2.c and 2.e).

In all cases, a backthrust is generated (Figure 2.a-f). Initially, it exhibits a dipping angle similar to the LVZ (Figures 2.a and 2.c). Both structures have a dipping angle of approximately 35º (e.g., Figure 2.a). However, as the FE model evolves, the backthrust maintains its dipping angle, while the LVZ exhibits a higher angle of around 42º (Figure 2.b). The FE model with a cover sequence of 10^{20} Pa s, in its final stage, is the only one that reveals the presence of the main reverse fault, the LVZ, and two parallel backthrusts (Figure 2.b). This new backthrust forms a conjugate system with the LVZ (Figure 2.b). When the viscosity of the cover layers is set to 10^{20} Pa s, they thin out more in the anticline hinge, leading to a thickening of the associated synclines (Figure 2.b).

Insert Figure 2 here.

3.1.2 Fault angle of 25º - 35º

Simulations involving deeper dipping fault angles (Figure 2.g-r) show fewer structures compared to the previously described models (Figure 2.a-f). FE models with a fault angle of 25º (Figure 2.g-l) exhibit more symmetrical folds compared to the 15º fault simulations. The most symmetrical structures are obtained with a 35º fault angle, regardless of the viscosity used in the cover layers (Figure 2.m-r). The resulting anticline shows a symmetric shape with a closed hinge (e.g., Figure 2.p). The thickness of the backthrust increases as the viscosity of the cover layers and the dipping angle of the reverse fault increase (Figure 2.r).

In the simulations with cover viscosity of 10^{20} Pa s, the cover layers thin out in the anticline hinge, while the frontal syncline exhibits greater thickness (Figures 2.h and 2.n). In contrast, the remaining cases (Figures 2.j, 2.l, 2.p, and 2.r), where the viscosity values of the cover layers are higher, do not exhibit this characteristic. The same thinning of the cover layer was observed in the previous suite (Figure 2.b).

3.2. Kinematic evolution of the models

Insert Figure 3 here.

3.2.1 Fault angle of 15º

In terms of velocity, the thrust exerted by the LVZ (Figure 2.a-f) determines the orientation of the velocity vectors (e.g., Figures 3.a and 3.b), unlike the other cases (Figure 3.g-r), where the vectors primarily follow the main ramp (e.g., Figures 3.o and 3.p).

Two distinct patterns are observable depending on the viscosity of the cover layers (Figure 3.a-f). Models with cover layers having a viscosity of 10^{20} Pa s (Figures 3.a and 3.b) show higher velocity values located in the forelimb, with velocity vectors parallel to the LVZ (~10^{21} Pa s). In the final stage, the velocity magnitude in the upper sector of the forelimb reaches the highest values (1.5 cm/yr) among all simulations involving 15º as the fault angle (Figure 3.b). Even the most distant portion of the folding, at 100 kilometers, is affected (Figure 3.b). In the backlimb, the top layers exhibit low velocities (0.4 cm/yr) (Figure 3.a). Similarly, low velocity values (0.3 cm/yr) are evident in the region between the reverse fault and the LVZ (Figures 3.a-d). The kinematic field suggests that the deformation in this sector is insignificant; despite being part of the imposed hanging block, it behaves like a footwall (Figures 3.b and 3.d). Models with a viscosity set to 10^{22} Pa s (Figures 3.e and 3.f) display a progressive pattern of velocity vector rotation, becoming semi-parallel to the main reverse fault, as expected for theoretical trishear behavior. The progressive rotation of the velocity vectors is more pronounced in the model with a viscosity of 10^{22} Pa s (Figure 3.f).

3.2.2 Fault angle of 25º - 35º

Simulations involving a 25º fault (Figure 3.g-l) show distribution trend similar to that reported in the earlier suite for the kinematic field (Figure 3.f), particularly when the viscosity of the cover layers is set to 10^{21}-10^{22} Pa s (Figures 3.j and 3.l). The velocity vectors tend to align parallel to the main reverse fault, and a new clockwise rotation is observed in the forelimb from the tip of the fault to the footwall of the structure (e.g., Figure 3.j). The FE model with cover layers' viscosity set at 10^{20} Pa s displays velocities ranging from 1.0 to 1.5 cm/yr in the forelimb region (Figures 3.g and 3.h). The backlimb region presents low velocity (0.4 cm/yr) (Figure 3.g). Similar to the 15º suite (Figure 3.b), the deformation affects the folding's most distant area of the fold, which is 100 kilometers away from the moving wall (Figure 3.h).

Two different trends are observed depending on the viscosity used in simulations involving the 35º fault (Figure 3.m-r). In cases where the layers are mechanically stronger (viscosity equal to or greater than 10^{21} Pa s; Figure 3.o-r), the velocity vectors in the hanging wall become parallel to the ramp as the fold evolves. The rotation from the tip point of the fault to the footwall, where velocity is close to zero, is clearly visible from the initial stage (Figure 3.o). In the FE model where the viscosity of the cover layers is lower (Figures 3.m and 3.n), the velocity vectors also align parallel to the main ramp as the fold evolves, but two distinct features are identified: closer to the backthrust, in the upper sector of the backlimb, there is a relative minimum (~0.5 cm/yr, Figure 3.m), and in the upper sector of the forelimb, there is a maximum (~1.2 cm/yr, Figure 3.n). In this case, no progressive rotation is identified (Figures 3.m and 3.n).

3.3 Comparison with Trishear/apical angle values

For the comparison of each obtained fault-propagation fold with the theoretical trishear kinematic model, the initial stage of the FE models was utilized (Figures 2 and 3, 0.4 Myr). Subsequent stages involved the further displacement of the main fault and its interaction with the cover layers, resulting in modifications to the kinematic field. To ensure an accurate comparison, the displacement at each selected step was carefully measured and inputted as a parameter in Andino 3D. Special attention was given to the apical angle parameter. During the initial stages of the FE models, it was observed that fault propagation across the cover layers does not contribute to the rupture of the material. As a result, the P/S values from the FE simulations remain relatively low at the selected stage for kinematic comparison.

To compare each FE model with the trishear method (taking into account fault angle, slip, and P/S), the apical angle was tested at intervals of 5 degrees (ranging from 20^{o} to 85^{o}). The difference between the velocity field of the FE model and the theoretical trishear model was calculated to determine the trishear apical angle that best approximates the numerical kinematic field in the folds. This approach allowed finding the best fit (Table 2). Subsequently, the magnitude and angular differences between the trishear method and the FE simulations were computed after scaling the vectors.

Since the geometric and kinematic evolution (Figure 2 and 3) of theFE models with a reverse fault at 25^{o} and 35^{o} are extremely similar, the decision was made to focus on the 25^{o} scenario, as it represents a more typical dipping angle in natural fault-propagation folds and reverse faults (Mitra, 1990; Sibson and Xie, 1998).

Insert Table 2 here.

Insert Figure 4 here.

Figure 4 presents the absolute difference in velocity magnitudes between FE models with a fault angle of 15º and 25º and the trishear method. Generally, FE models with a 15º fault angle exhibit larger disparities compared to the trishear method. The greatest differences (~0.9 cm/yr) occur within the reverse fault zone for the three models (Figure 4.a-c). Significant discrepancies are also observed in the backthrust located in the backlimb of the structure, particularly in the FE model with a viscosity of 10^{20} Pa s. In this case, the trishear method provides a better approximation of the velocity in the upper sector of the hanging wall, and in the forelimb. Lower values are also observed surrounding the forelimb (Figure 4.a). The other two FE simulations with the cover layers viscosities set at $10^{21,}$ and 10^{22} Pa s show a similar pattern (Figure 4.b-c).

Compared to the 15º fault FE models, the kinematic fields in the FE models with a 25º fault angle show a better fit with the trishear method (Figure 4.d-f). The region near the main reverse fault shows the largest differences (~0.7 cm/yr). The FE model with the weakest cover layers (Viscosity = 10^{20} Pa s) shows the lowest discrepancies with the trishear method, particularly in the forelimb area and the trishear zone where the difference approaches zero (Figure 4.d). However, higher values are observed in the upper zone of the backlimb (~0.55 cm/yr), while the remaining FE models exhibit differences of approximately ~0.30 cm/yr (Figures 4.e-f).

Insert Figure 5 here.

Figure 5 shows the angular difference of the velocity vectors between FE and trishear models. In the first suite of FE models, the most substantial differences are observed within the hanging wall (-40º) (Figure 5.a-c). However, closer to the main reverse fault, within a small zone of approximately 5 km, the differences are significantly lower (-10º). This characteristic can be identified in Figures 5.a-b but is not evident in the model with a cover layer viscosity set of 10^{22} Pa s (Figure 5.c). Additionally, there is a region of ~20 km to the left of the trishear zone in the forelimb where the differences are also diminished. Particularly, in the FE model with a viscosity of 10^{20} Pa s, the differences tend to be zero (Figure 5.a).

In the 25^{o} suite, the differences inside the trishear zone range from approximately -5^{o} to 5^{o}. However, the FE models exhibit noticeable deviations from the theoretical trishear particularly in the backlimb (Figure 5.d-f). Notably, the FE model with a viscosity of 10^{20} Pa s shows differences in the forelimb, situated to the left of the trishear zone (Figure 5.d). This area introduces differences of approximately 10^{o} to 20^{o}, which are absent in the other simulation (Figures 5.e-f). Conversely, the FE models with a cover layer viscosities of 10^{21} and 10^{22} Pa s yield a better approximation, particularly in the forelimb region. The FE model with the viscosity of 10^{22} Pa s shows differences in the area located to the left of the backthrust (Figure 5.f). Unlike the other FE models in this suite (Figures 5.d-e), the resulting difference is smaller ($\sim 15^{o}$).

4. Discussion

The trishear method presents challenges in characterizing several parameters (Coleman et al., 2019). Previous studies suggest that in the early stages of faulting, regardless of fault type (reverse or normal), the P/S ratios are approximately equal to one (Shi and Ling, 2022). As time progresses, fault ruptures gradually propagate into the overlying rock, resulting in an increased P/S ratio. In this study, tests were conducted by varying the P/S values within the range of 1 to 2.

4.1 Effect of viscosity on the velocity fields:

Viscosity plays a crucial role in determining the deformation style and velocity field of fault-propagation folds in the simulations. As the viscosity of the cover layers affected by folding increases, the estimated apical angle decreases.

The apical angle controls the extent of the deformation zone above the fault plane. Lower apical angle values explain localized deformation in materials with higher viscosity. Plotek et al. (2022) described similar tendencies in fault-propagation folding models with layers resembling evaporites, where lower viscosities are best approximated by the trishear model corresponding to high apical angle values of 60°–70°.

The geometry of the folds formed in the cover layers with a viscosity of 10^{20} Pa s is notable. In the anticline hinge, the upper layer thins out, leading to the thickening of associated synclines (Figures 2.b, 2.h, and 2.n). Previous research supports the idea that weak or incompetent units in the synclines undergo thickness during deformation, resulting in folding (Laubach et al., 2009; Mou et al., 2023). Although the finite element models used in this study are simplified without considering mechanical behavior alternation, similar findings to previous studies on heterogeneous sequences were obtained.

Regarding the velocity, the models incorporating cover layers with 10^{20} Pa viscosity demonstrate a kinematic field analogous to that predicted in fault-bend folds, where the material translation occurs over a thrust ramp (Suppe, 1983). Simulations with a viscosity of 10^{22} Pa s, follow the trishear kinematic pattern (Figures 3.l and 3.r). The trishear method proves useful for approximating the kinematic field in fault-propagation folds (Hughes and Shaw, 2014; Pei et al., 2017; Li et al., 2020; He et al., 2021). However, in nearly all simulations, it is evident that the imposed velocity decreases at a faster rate than the suggested by the theoretical trishear method (Figure 4). Regarding the angle differences, the largest discrepancies (~40°) are associated with the backthrust, which is present in all the finite element models.

On the other hand, in the suite with a fault angle set at 15°, the highest velocity differences are observed near the main reverse fault in the hanging wall, indicating limited deformation of the material (Figure 4.a-c). Velocity discrepancies of ~0.9 cm/yr can be attributed to numerical velocity vectors being close to zero. This finding can be explained by the development of the LVZ, which acts as the actual reverse fault (Figures 2.a, 2.c, and 2.e). The fault imposed by the model's configuration becomes secondary, and the kinematic field responds to this new structure (Figure 3.a, 3.c, and 3.e). Consequently, the region between the LVZ and the main reverse ramp behaves akin to a footwall. This accounts for the larger differences observed in this area and the lower values (-10°) in proximity to the ramp (Figure 4.a-c and Figure 5.a-b). It is important to note that the LVZ was only observed in models with a fault dipping angle set to 15º, and this characteristic will be further discussed in the following section.

4.2 Effect of the fault angle in the finite element simulations

A distinct zone known as the low viscosity zone (LVZ) emerges as a notable feature in the finite element simulations conducted in this study, particularly when the main reverse fault angle is set to 15º. Remarkably, the LVZ assumes the role of the primary fault and governs the evolution of the kinematic field, effectively surpassing the reverse fault imposed based on plasticity parameters within the finite element simulation setup.

To gain insight into this phenomenon, a series of fracture experiments was performed using Underworld2. Triaxial tests were conducted on samples of basement rock to accurately represent its mechanical properties in the finite element models (Faizi et al., 2020; You et al., 2021). These tests were carried out under varying confining pressures, simulating depths ranging from 5.0 to 17.5 km. Subsequently, the resulting fault angles were measured, and the stress tensor components from the numerical model results were extracted. In this way, it was possible to derived the stress tensor from the model. Based on this information, the shear and normal stresses acting on the measured fault were calculated. Figure 6 presents the envelope obtained for the intact basement rock in the finite element simulations (blue line, Figure 6). The values of normal stress and shear stress are observed for each of the conducted triaxial compression tests (Figure 6). Notably, this envelope closely approximates the Mohr-Coulomb failure criteria (Labuz and Zang, 2012; Heyman et al., 1972).

Insert Figure 6 here.

Mohr-Coulomb states that a material will fail when the shear stress (τ) on a plane reaches a critical value dependent on the normal stress (σ_n) on that same plane. Mathematically, it is expressed as (Eq. 1):

$$\tau = c + \sigma_n \cdot \tan(\phi) \qquad \text{(Equation 1)}$$

τ is the shear stress, c is the cohesion of the material (shear strength under zero normal stress conditions), σ_n is the normal stress, and ϕ is the internal friction angle of the material. In a Mohr diagram, this criterion is represented as a Mohr circle where the horizontal axis represents normal stresses and the vertical axis represents shear stresses.

The determination of the Mohr-Coulomb circle was based on the major stress values obtained from the stress tensor of the finite element simulations of fault-propagation folds, with the top of the basement situated at a depth of 7.5 km. The calculated circle closely aligns with the results obtained from the mechanical testing, providing validation for the approach.

Subsequently, an investigation was conducted to examine the behavior within a zone of extremely low cohesion when the rock already possessed a fracture. In cases where the fault has an angle less than 23^o, as indicated by the intersection of the circle and the line representing cohesion close to zero, the pre-existing fault does not reactivate; instead, it generates a new one fault following the envelope of the intact basement rock. This observation is consistent with the findings of the finite element models, where the 15^o fault did not reactivate. Instead, the system produced a new fault at approximately 33^o corresponding to the LVZ. The viscosity values (~10^{21} Pa s) in this newly formed fault closely resemble those assigned to the imposed main reverse fault. The angle indicated in the Mohr-Coulomb circle at its intersection with the previously calculated experimental values is 34^o (Figure 6, blue line).

4.3 Experimental limitations

The constitutive behavior of rocks is governed by various deformation mechanisms influenced by factors such as phase content, chemical composition, and thermodynamics (Burgmann and Dresen, 2008). In this study, the rocks are assumed to be homogeneous rheological layers. The materials in the model are assigned a Newtonian rheology, as viscous diffusion and dislocation creep can be neglected under the pressures and temperatures considered and isoviscous layers are used (Holt and Condit, 2021; Schmid et al., 2023). The simulations consider temperature and pressure-dependent densities, but do not incorporate phase changes or associated chemical processes. Overall, these simulations provide valuable insights into the behavior of the trishear kinematic model for fault-propagation folding.

The present study acknowledges the inherent limitations associated with the employed trishear theoretical model. Some of the limitations of trishear are intrinsic to kinematic models that neglect the mechanical properties of the rock. Additionally, it assumes a consistent parallel movement of vectors within the hanging block along the reverse fault, typically characterized by planar-ramp geometries. Furthermore, this approach overlooks the deformation inside the hanging wall and backlimb of the structure; however, it is important to note that this model has been widely accepted and utilized in numerous instances.

The trishear kinematics are specifically formulated to model the distortion ahead of a propagating fault, apart from the translation along the fault. The acknowledgment of its kinematic nature and its widespread use in the scientific community is clear. Still, it is essential to recognize that, by focusing on mechanical variations within the beds during folding, additional insights can be gained that go beyond the scope of trishear's kinematic representation. The intention is not to undermine the utility of trishear but rather to complement its insights with a consideration of mechanical aspects for a more comprehensive understanding of fault-propagation folds.

5. Conclusions

In this study, finite element models were developed in this study to investigate fault-propagation folding and to examine the influence of the rheology of the cover layers and the fault dipping angle on the kinematic field of the resulting fold. The results were then compared with the trishear theoretical model.

Observed deviations from the trishear model increase with the weakness of the cover layers. However, these discrepancies could be approximated by using higher apical angles. Additionally, simulations with gentler fault angles exhibited greater differences from the trishear model. In the suite of models with a fault angle set at 15º, a frontal syncline located behind the main reverse fault was observed. This asymmetry was particularly pronounced in simulations where the cover layers had a viscosity of 10^{20} Pa s. These simulations revealed the development of a mechanically weaker discontinuity characterized by a low viscosity zone, characterized by viscosities around 10^{21} Pa s. The presence of the LVZ induced faulting and absorbed slip, leading to deviations of the velocity vectors from parallel alignment with the main reverse ramp.

In models with fault angles set at 25° or 35°, the behavior is closely aligned with the predictions of the theoretical models, featuring velocity vectors parallel to the fault ramps, progressive rotations, and symmetrical folds. However, in the case of cover layers with a viscosity of 10^{20} Pa s, the highest velocities were observed in the forelimb. This observation could be attributed to material migration toward the synclines.

The apical angle plays a critical role in determining the size and shape of the deformation zone above the fault plane in fault-propagation folding. It is strongly influenced by the viscosity of the materials involved. Lower apical angles correspond to more localized deformation, which occurs in materials with higher viscosity. Both the angle of the reverse fault and the viscosity of the folded layers significantly contribute to the resulting geometry and kinematics of the fault-propagation fold.

Acknowledgments

This study has been funded by the grant PICT-2019-0997 from the Agencia Nacional de Promoción Científica y Tecnológica. Special thanks are extended to LA.TE. Andes for generously providing the academic license of Andino 3D software. The authors would also like to express their appreciation to the Instituto de Estudios Andinos Don Pablo Groeber (IDEAN), Consejo Nacional de Investigaciones Científicas y Técnicas (CONICET), and the Universidad de Buenos Aires (UBA) for their valuable support during the course of this research.

References:

Ahumada, E.A., Costa, C., Gardini, C.E., & Diederix, H. (2006). La estructura del extremo sur de la Sierra de Las Peñas-Las Higueras, Precordillera de Mendoza. Assoc. Geol. Arg., 6, 11–17.

Allmendinger, R.W. (1998). Inverse and forward numerical modeling of trishear fault propagation folds. Tectonics, 17, 640–656. https://doi.org/10.1029/98TC01907

Allmendinger, R.W., Cardozo, N.C., & Fisher, D. (2012). Structural Geology Algorithms: Vectors & Tensors. Cambridge, England: Cambridge University Press.

Allmendinger, R.W., Zapata, T., Manceda, R., & Dzelalija, F. (2004). Trishear kinematic modeling of structures, with examples from the Neuquén Basin, Argentina. AAPG Memoir, 356–371. https://doi.org/10.1306/m82813c19

Barton, N. (2013). Shear strength criteria for rock, rock joints, rockfill and rock masses: problems and some solutions. J. Rock Mech. Geotech. Eng. 5/4, 249–261. http://dx.doi.org/10.1016/j.jrmge.2013.05.008

Beucher, R., Moresi L., Giordani, J., Mansour J., Sandiford, D., Farrington, R., Mondy, L., Mallard, C., Rey, P., Duclaux, G., Kaluza, O., Laik, A., & Morón, S. (2019). UWGeodynamics: A Teaching and Research Tool for Numerical Geodynamic Modelling. Journal of Open Source Software. https://doi.org/10/gf9rmd

Bonanno, E., Bonini, L., Basili, R., Toscani, G., & Seno, S. (2017). How do horizontal, frictional discontinuities affect reverse fault-propagation folding? Journal of Structural Geology, 102, 147–167. https://doi.org/10.1016/j.jsg.2017.08.001

Brandes, C., & Tanner, D.C. (2014). Fault-related folding: A review of kinematic models and their application. Earth-Science Reviews. https://doi.org/10.1016/j.earscirev.2014.06.008

Bürgmann, R., & Dresen, G. (2008). Rheology of the Lower Crust and Upper Mantle: Evidence from Rock Mechanics, Geodesy, and Field Observations. Annual Review of Earth and Planetary Sciences, 36(1), 531–567. https://doi.org/10.1146/annurev.earth.36.031207.124326

Capitanio, F.A., Nebel, O., & Cawood, P.A. (2020). Thermochemical lithosphere differentiation and the origin of cratonic mantle. Nature, 588, 89–94. https://doi.org/10.1038/s41586-020-2976-3

Cardozo, N. (2005). Trishear modeling of fold bedding data along a topographic profile. Journal of Structural Geology, 27(3), 495–502. https://doi.org/10.1016/j.jsg.2004.10.004

Cardozo, N., & Aanonsen, S. (2009). Optimized trishear inverse modeling. Journal of Structural Geology, 31, 546–560. https://doi.org/10.1016/j.jsg.2009

Cardozo, N., Bhalla, K., Zehnder, A.T., & Allmendinger, R.W. (2003). Mechanical models of fault propagation folds and comparison to the trishear kinematic model. Journal of Structural Geology, 25, 1–18. https://doi.org/10.1016/S0191-8141(02)00013-5

Cenki-Tok, B., Rey, P.F., & Arcay, D. (2020). Strain and retrogression partitioning explain long-term stability of crustal roots in stable continents. Geology, 48, 658–662. https://doi.org/10.1130/G47301.1

Coleman, A.J., Duffy, O.B., & Jackson, C.A.L. (2019). What is Trishear? Retrieved from https://doi.org/10.31223/OSF.IO/UZHKR

Cristallini, E.O., & Allmendinger, R.W. (2001). Pseudo 3-D modeling of trishear fault-propagation folding. Journal of Structural Geology, 23, 1883–1899. https://doi.org/10.1016/S0191-8141(01)00034-7

Cristallini, E., Sanchez, F., Balciunas, D., Mora, A., Ketcham, R., Nigro, J., Hernández, J., & Hernandez, R. (2021). Seamless low-temperature thermochronological modeling in Andino 3D, towards integrated structural and thermal simulations. Journal of South American Earth Sciences, 105. https://doi.org/10.1016/j.jsames.2020.102851

Davis, R. O., & Selvadurai, A. P. S (2002). Plasticity and Geomechanics, Cambridge University Press.

Erslev, E. A. (1991). Trishear fault-propagation folding. Geology, 19(6), 617-620.

Faizi, S.A., Kwok, C.Y., & Duan, K. (2020). The effects of intermediate principle stress on the mechanical behavior of transversely isotropic rocks: Insights from DEM simulations. International Journal for Numerical and Analytical Methods in Geomechanics, 44, 1262–1280. https://doi.org/10.1002/nag.3060

Gianni, G.M., Likerman, J., Navarrete, C.R., Gianni, C.R., & Zlotnik, S. (2023). Ghost-arc geochemical anomaly at a spreading ridge caused by supersized flat subduction. Nature Communications, 14, 2083. https://doi.org/10.1038/s41467-023-37799-w

Grothe, P.R., Cardozo, N., Mueller, K., & Ishiyama, T. (2014). Propagation history of the Osaka-wan blind thrust, Japan, from trishear modeling. Journal of Structural Geology, 58, 79–94. https://doi.org/10.1016/j.jsg.2013.10.014

Hardy, S. (2019). Discrete element modelling of extensional, growth, fault-propagation folds. Basin Research, 31, 584–599. https://doi.org/10.1111/bre.12335

Hardy, S., & Allmendinger, R.W. (2011). Trishear: A review of kinematics, mechanics, and applications. AAPG Memoir. https://doi.org/10.1306/13251334M943429

Hardy, S., & Finch, E. (2007). Mechanical stratigraphy and the transition from trishear to kink-band fault-propagation fold forms above blind basement thrust faults: A discrete-element study. Marine and Petroleum Geology, 24, 75–90. https://doi.org/10.1016/j.marpetgeo.2006.09.001

Hardy, S., & Ford, M. (1997). Numerical modeling of trishear fault propagation folding. Tectonics, 16, 841–854. https://doi.org/10.1029/97TC01171

He, J., La Croix, A.D., Gonzalez, S., Pearce, J., Ding, W., Underschultz, J.R., & Garnett, A. (2021). Quantifying and modelling the effects of pre-existing basement faults on folding of overlying strata in the Surat Basin, Australia: implications for fault seal potential. Journal of Petroleum Science and Engineering, 198, 108207. https://doi.org/10.1016/j.petrol.2020.108207

Heyman, J., de Coulomb, C.A., & Coulomb, C.A. (1972). Coulomb's memoir on statics: An essay in the history of civil engineering. CUP Archive

Holt, A.F., & Condit, C.B. (2021). Slab temperature evolution over the lifetime of a subduction zone. Geochemistry, Geophysics, Geosystems, 22(6). https://doi.org/10.1029/2020GC009476

Hughes, A. N., & Shaw, J. H. (2014). Fault displacement-distance relationships as indicators of contraction fault-related folding style. AAPG Bulletin, 98, 227–251. https://doi.org/10.1306/05311312006

Hughes, A. N., & Shaw, J. H. (2015). Insights into the mechanics of fault-propagation folding styles. Bulletin of the Geological Society of America, 127, 1752–1765. https://doi.org/10.1130/B31215.1

Hughes, A., Benesh, N. P., & Shaw, J. H. (2014). Factors that control the development of fault-bend versus fault-propagation folds: insights from mechanical models based on the discrete element method (DEM). Journal of Structural Geology, 68, 121–141.

Jabbour, M., Dhont, D., Hervouët, Y., & Deroin, J. P. (2012). Geometry and kinematics of fault-propagation folds with variable interlimb angle. Journal of Structural Geology, 42, 212–226. https://doi.org/10.1016/j.jsg.2012.05.002

Ju, W., Zhong, Y., Liang, Y., Gong, L., Yin, S., & Huang, P. (2023). Factors influencing fault-propagation folding in the Kuqa Depression: Insights from geomechanical models. Journal of Structural Geology. https://doi.org/10.1016/j.jsg.2023.104826

Khalifeh-Soltani, A., Alavi, S. A., Ghassemi, M. R., & Ganjiani, M. (2021). Geomechanical modelling of fault-propagation folds: estimating the influence of the internal friction angle and friction coefficient. Tectonophysics. https://doi.org/10.1016/j.tecto.2021.228992

Meng, Q., & Hodgetts, D. (2019). Combined control of décollement layer thickness and cover rock cohesion on structural styles and evolution of fold belts: a discrete element modelling study. Tectonophysics, 757, 58–67. https://doi.org/10.1016/j.tecto.2019.03.004

Mitra, S. (1990). Fault-propagation folds: geometry and kinematic evolution, and hydrocarbon traps. AAPG Bulletin, 74, 921–945. https://doi.org/10.1306/0C9B23CB-1710-11D7-8645000102C1865D

Mitra, S., & Miller, J. F. (2013). Strain variation with progressive deformation in basement-involved trishear structures. Journal of Structural Geology, 53, 70–79. https://doi.org/10.1016/j.jsg.2013.05.007

Mitra, S., & Mount, V. S. (1998). Foreland basement–involved structures. American Association of Petroleum Geologists Bulletin, 82, 70–109.

Mou, Y., Guo, W., & Pei, Y. (2023). A new method to evaluate the effects of mechanical heterogeneity on fault architecture in sedimentary sequences. Natural Gas Industry B. https://doi.org/10.1016/j.ngib.2023.03.001

Moresi, L. N., Dufour, F., & Mühlhaus, H. B. (2003). A Lagrangian integration point finite element method for large deformation modelling of viscoelastic geomaterials. Journal of Computational Physics, 184, 476–497. https://doi.org/10.1016/S0021-9991(02)00031-1

Moresi, L., Quenette, S., Lemiale, V., Mériaux, C., Appelbe, B., & Mühlhaus, H. B. (2007). Computational Approaches to Studying Non-Linear Dynamics of the Crust and Mantle. Physics of the Earth and Planetary Interiors, Computational Challenges in the Earth Sciences, 163(1), 69–82. https://doi.org/10.1016/j.pepi.2007.06.009

Labuz, J. F., & Zang, A. (2012). Mohr–Coulomb Failure Criterion. Rock Mechanics and Rock Engineering, 45, 975–979. https://doi.org/10.1007/s00603-012-0281-7

Laubach, S. E., Olson, J. E., & Gross, M. R. (2009). Mechanical and fracture stratigraphy. AAPG Bulletin, 93(11), 1413–1426. https://doi.org/10.1306/07270909094

Li, Z., Chen, W., Jia, D., Sun, C., Zheng, W., Zhang, P., Wang, W., Li, T., & Xiong, J. (2020). The effects of fault geometry and kinematic parameters on 3D fold morphology: insights from 3D geometric models and comparison with the Dushanzi anticline, China. Tectonics, 39.

Likerman, J., Zlotnik, S., & Li, C. F. (2021). The effects of small-scale convection in the shallow lithosphere of the North Atlantic. Geophysical Journal International, 227(3), 1512–1522. https://doi.org/10.1093/gji/ggab286

Liu, C., Yin, H., & Zhu, L. (2012). TrishearCreator: a tool for the kinematic simulation and strain analysis of trishear fault-propagation folding with growth strata. Computers & Geosciences, 49, 200–206. https://doi.org/10.1016/j.cageo.2012.07.002

Oakley, D. O., & Fisher, D. M. (2015). Inverse trishear modeling of bedding dip data using Markov chain Monte Carlo methods. Journal of Structural Geology, 80, 157–172.

Pace, P., Calamita, F., & Tavarnelli, E. (2022). Along-strike variation of fault-related inversion folds within curved thrust systems: the case of the Central-Northern Apennines of Italy. Marine and Petroleum Geology, 142, 105731. https://doi.org/10.1016/j.marpetgeo.2022.105731

Pei, Y., Paton, D. A., & Knipe, R. J. (2014). Defining a 3-dimensional trishear parameter space to understand the temporal evolution of fault propagation folds. Journal of Structural Geology, 66, 284–297. https://doi.org/10.1016/j.jsg.2014.05.018

Pei, Y., Paton, D. A., Wu, K., & Xie, L. (2017). Subsurface structural interpretation by applying trishear algorithm: An example from the Lenghu5 fold-and-thrust belt, Qaidam Basin, Northern Tibetan Plateau. Journal of Asian Earth Sciences, 143, 343–353.

Plotek, B., Heckenbach, E., Brune, S., Cristallini, E., & Likerman, J. (2022). Kinematics of fault-propagation folding: analysis of velocity fields in numerical modeling simulations. Journal of Structural Geology, 162, 104703. https://doi.org/10.1016/j.jsg.2022.104703

Reston, T. (2020). On the rotation and frictional lock-up of normal faults: Explaining the dip distribution of normal fault earthquakes and resolving the low-angle normal fault paradox. Tectonophysics, 790, 228550. https://doi.org/10.1016/j.tecto.2020.228550

Rey, P. F., Mondy, L., Duclaux, G., Teyssier, C., Whitney, D. L., Bocher, M., & Prigent, C. (2017). The origin of contractional structures in extensional gneiss domes. Geology, 45, 263–266. https://doi.org/10.1130/G38595.1

Schmid, T. C., Brune, S., Glerum, A., & Schreurs, G. (2023). Tectonic interactions during rift linkage: insights from analog and numerical experiments. Solid Earth, 14(4), 389-407.

Shi, J., & Ling, D. (2022). A trishear model with self-adaptive propagation-to-slip ratio. Journal of Structural Geology, 159. https://doi.org/10.1016/j.jsg.2022.104602

Sibson, R. H., & Xie, G. (1998). Dip range for intracontinental reverse fault ruptures: truth not stranger than friction? Bulletin of the Seismological Society of America, 88, 1014–1022.

Smith, T., Rosenbaum, G., & Gross, L. (2021). Formation of oroclines by buckling continental ribbons: Fact or fiction? Tectonophysics, 814, 228950. https://doi.org/10.1016/j.tecto.2021.228950

Storti, F., Salvini, F., & McClay, K. (1997). Fault-related folding in sandbox analogue models of thrust wedges. Journal of Structural Geology, 19, 583–602. https://doi.org/10.1016/S0191-8141(97)83029-5

Suppe, J. (1983). Geometry and kinematics of fault-bend folding. American Journal of Science, 283, 684–721.

Suppe, J., & Medwedeff, D. A. (1984). Fault-propagation folding. Geological Society of America Abstracts with Programs, 16, 670.

Suppe, J., & Medwedeff, D. A. (1990). Geometry and kinematics of fault-propagation folding. Eclogae Geologicae Helvetiae, 83, 409–454.

Treffeisen, T., Henk, A. (2020). Representation of faults in reservoir-scale geomechanical finite element models – A comparison of different modelling approaches. J. Struct. Geol., 131. https://doi.org/10.1016/j.jsg.2019.103931

You, W., Dai, F., Liu, Y., Du, H. B., & Jiang, R. C. (2021). Investigation of the influence of intermediate principal stress on the dynamic responses of rocks subjected to true triaxial stress state. International Journal of Mining Science and Technology, 31(5), 913–926.

Zehnder, A., & Allmendinger, R. (2000). Velocity field for the trishear model. Journal of Structural Geology, 22, 1009–1014. https://doi.org/10.1016/S0191-8141(00)00037-7.

Figure Captions

Figure 1: Finite element model setup. The moving wall is represented as a gray rectangle.

Figure 2: Geometrical evolution of the FE models with fault angles of 15° (a-f), 25° (g-l) and 35° (m-r). The panels depict viscosity. Two time-steps are selected for each simulation: 0.4 and 1.0 Myr. Each column displays the viscosity for the cover layers: 10^{20}, $10^{21,}$ and 10^{22} Pa s. The moving wall is indicated in gray and the white line represents the bottom of the upper sedimentary layer.

Figure 3: Kinematic evolution of the FE models with a 15°, 25° and 35° fault angle. The panels depict the velocity field with instantaneous velocity vectors relative to the footwall. Two time-steps are selected for each simulation: 0.4 and 1.0 Myr. Each column displays the viscosity for the cover layers: 10^{20}, 10^{21} and 10^{22} Pa s. The moving wall is indicated in gray.

Figure 4: Absolute difference in velocity fields between finite element and the theoretical trishear models. The red and blue arrows are the velocity vectors from the trishear and finite element models, respectively. Black fine lines indicate the apical angle used for the trishear method (Table 2). Thick black line is the main reverse fault.

Figure 5: Angular difference between the velocity vectors of the theoretical trishear and the finite element model (trishear - FE). Black fine lines indicate the apical angle applied for the trishear method (table 2). The thick black line is the main reverse fault. Red tones indicate higher angular values in the trishear theoretical model, whereas blue tones represent the opposite.

Figure 6: The Mohr-Coulomb circle constructed based on principal stresses obtained from the finite element tests. The green dots represent the results of normal stress and shear stress for each triaxial test. The blue and green lines correspond to the best fit for triaxial tests and tests without cohesion, respectively. The area enclosed by the intersections of the green line and the circle indicates the faulting angle. Faults with angles below 23^{o} will not undergo reactivation. In our FE simulations, with a 15^{o} fault, the main thrust is not reactivated. A new fault (LVZ) is generated following the angle of the envelope for the basement without previous weaknesses (blue line).

Tables

	Basement	Cover layers	Fault
Cohesion (MPa)	20	10	2
Angle of internal friction (º)	30	40	10
Density (kg/m³)	2700		
Viscosity (Pa s)	$1x10^{23}$	$1x10^{20}$ - 1×10^{22}	$1x10^{21}$
Fault angle (º)	from 15 to 35		

Table 1: Physical properties of the materials.

Viscosity of the layers (Pa s)	**Fault angle (º)**	
	15	25
	Apical angle for trishear method (º)	
1×10^{20}	80	60
1×10^{21}	45	50
1×10^{22}	30	30

Table 2: Best fit apical angle for each model.

Appendix

Numerical Modeling Method

We have developed a two-dimensional model to investigate the evolution of fault-propagation faults. The conservation equations for mass, momentum, and energy are systematically addressed within the framework of an incompressible, viscoplastic fluid confined to a 2D Cartesian domain. The numerical solution employs the finite element, particle-in-cell (PIC) methodology implemented in the Underworld2 code (Beucher *et al.,* 2019; Moresi *et al.,* 2003, 2007). Underworld2 adheres to a continuum mechanics approximation, a widely accepted method for delineating geological and geophysical phenomena. It adeptly addresses the conservation equations governing mass (Eq. 2), momentum (Eq. 3), and energy (Eq. 4).

$$\nabla . \mathrm{u} = 0$$

(Equation 2)

$$\rho Cp\left(\frac{\delta T}{\delta t} + u . \nabla\, T\right) = \nabla . k\nabla T + Q$$

(Equation 3)

$$\nabla . (\mathrm{n}\, \nabla\, \mathrm{u})\ -\ \nabla \mathrm{p} = -\rho \mathrm{g}$$

(Equation 4)

where u is the velocity, T is the temperature, t is time, Cp is the specific heat capacity, ρ is the density, k is the thermal conductivity, Q is an additional heat source for the energy equation, ∇ represents the gradient, η is the viscosity, g is the gravity force vector.

We use nonlinear temperature-dependent, and strain rate-dependent viscoplastic rheology. The viscous deformation of rocks is calculated using a temperature, pressure, and strain rate-dependent power-law equation. The viscosity for dislocation or diffusion creep (Eq. 5) is defined as:

$$\eta\ =\ \frac{1}{2} A^{-\frac{1}{n}}\, d^{\frac{m}{n}} \dot{\mathcal{E}}_{ii}^{\ \frac{1-n}{n}}\, exp\left(\frac{E + PV}{nRT}\right)$$

(Equation 5)

where η is the viscosity, *A* is the preexponential factor, *n* is the stress exponent, *E* is the activation energy, *P* is the pressure, *V* the activation volume, *R* the gas constant, *T* is the temperature at a given position, $\dot{\mathcal{E}}_{ii}$ is the square root of the second invariant of the strain rate tensor, *d* represents the grain size, and *m* is the grain size exponent. Viscosity is limited in the model between 10^{19} and 10^{24} Pa s. Maximum strain rates in the model reach ~10^{-14} s^{-1}, which produce a viscosity >10^{19} Pa s for the rheology used.

To transition to an isoviscous flow law, one simply sets the activation energy and activation volume to zero, employs an exponent equal to 1, a grain size exponent of 0, and a pre-exponential factor equal to 0.5 times the desired viscosity raised to the power of minus one. For instance, for a desired viscosity of 1 x 10^{19} Pa s, a pre-exponential factor of 0.5 x 10^{-19} should be utilized.

Plastic failure is determined using a pressure-dependent Drucker–Prager yield criterion (Davis and Selvadurai, 2002) (Eq. 6):

$$\sigma_y = C \cos(\text{Ø}) + P \sin(\text{Ø})$$

(Equation 6)

P is the pressure, *C* is the cohesión, Ø is the internal angle of friction.

A constant temperature (T = 293°C) is applied to the top boundary, with no heat flux across the side walls. The initial internal temperature distribution follows a lineal geothermal gradient until a temperature of 750°C is reached at the base of the model. The model uses a free-slip condition on the bottom boundary. The convergence velocity (1.2 cm/yr) is applied on the left wall. Particles in the footwall remain fixed (velocity = 0 cm/yr).

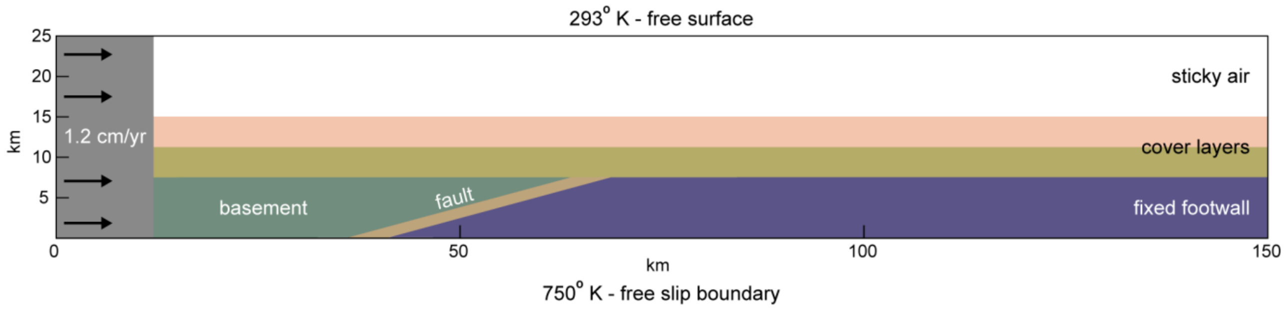

Figure 1: Finite element model setup. The moving wall is represented as a gray rectangle.

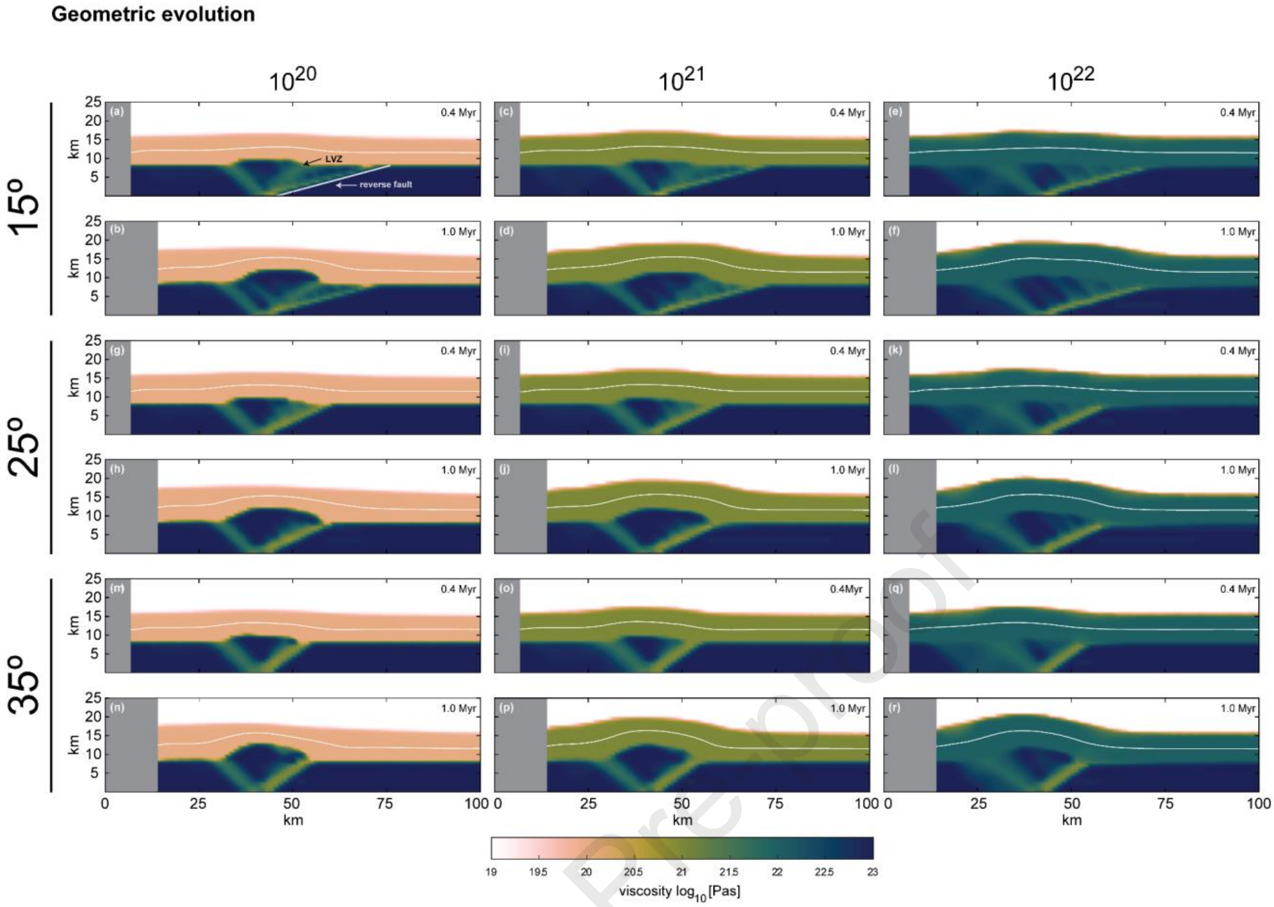

Figure 2: Geometrical evolution of the FE models with fault angles of 15° (a-f), 25° (g-l) and 35° (m-r). The panels depict viscosity. Two time-steps are selected for each simulation: 0.4 and 1.0 Myr. Each column displays the viscosity for the cover layers: 10^{20}, 10^{21}, and 10^{22} Pa s. The moving wall is indicated in gray and the white line represents the bottom of the upper sedimentary layer.

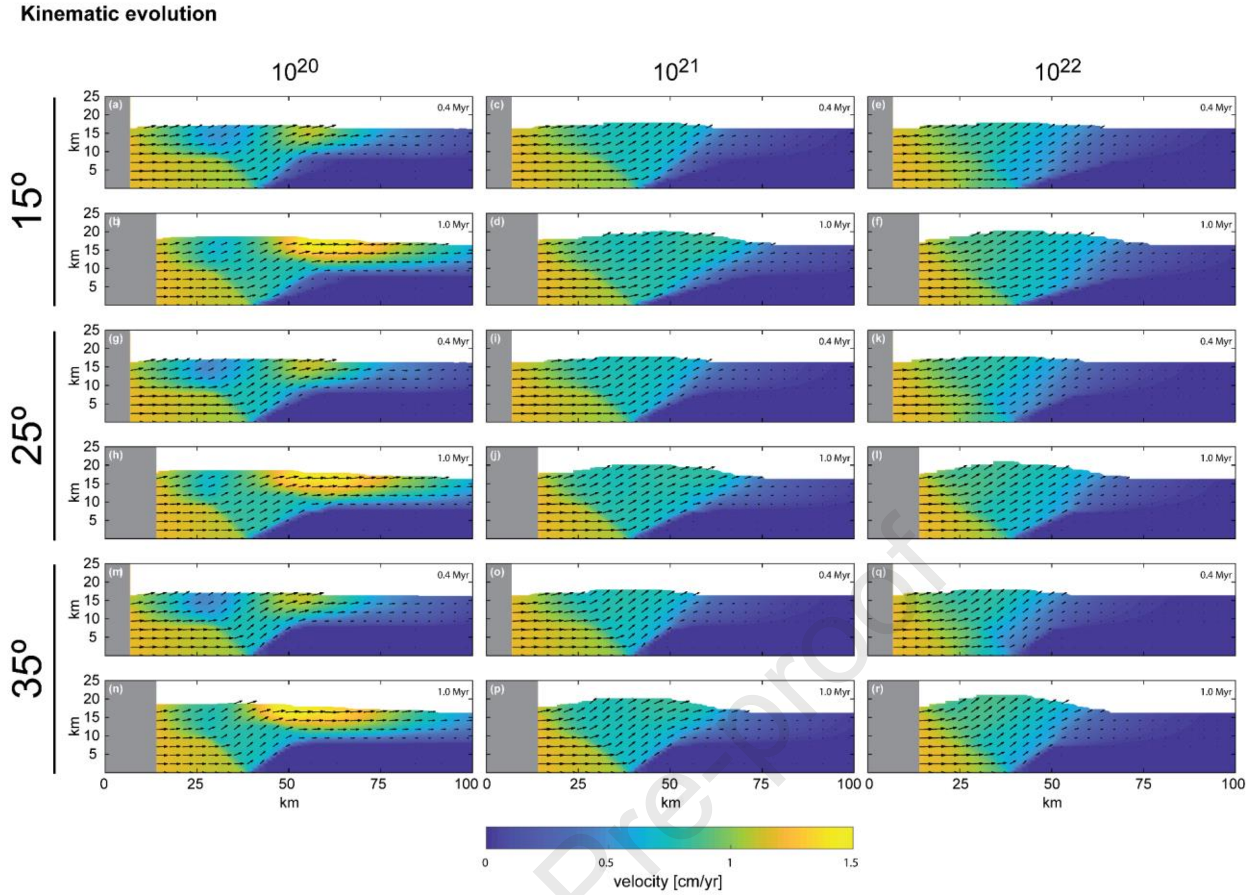

Figure 3: Kinematic evolution of the FE models with a 15°, 25° and 35° fault angle. The panels depict the velocity field with instantaneous velocity vectors relative to the footwall. Two time-steps are selected for each simulation: 0.4 and 1.0 Myr. Each column displays the viscosity for the cover layers: 10^{20}, 10^{21} and 10^{22} Pa s. The moving wall is indicated in gray.

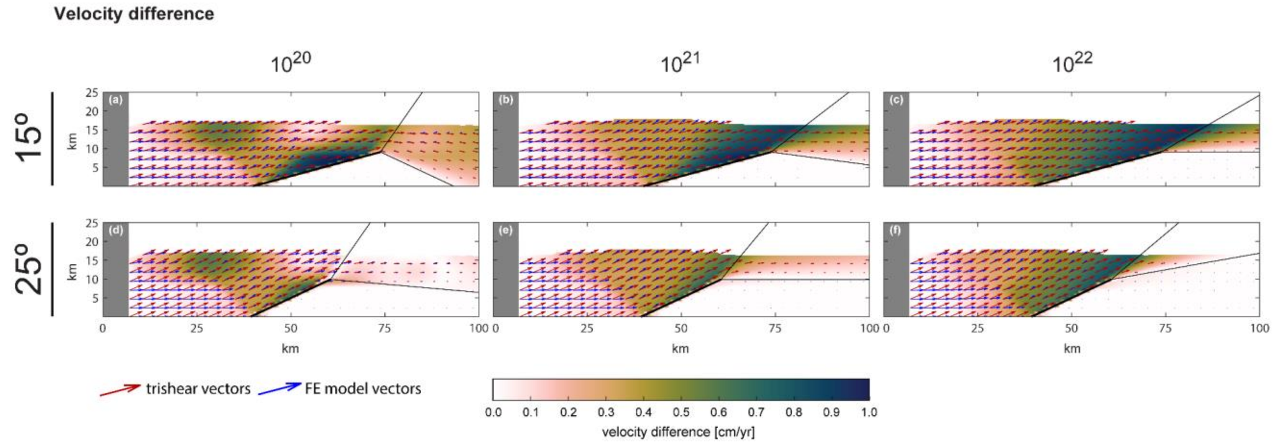

Figure 4: Absolute difference in velocity fields between finite element and the theoretical trishear models. The red and blue arrows are the velocity vectors from the trishear and finite element models, respectively. Black fine lines indicate the apical angle used for the trishear method (Table 2). Thick black line is the main reverse fault.

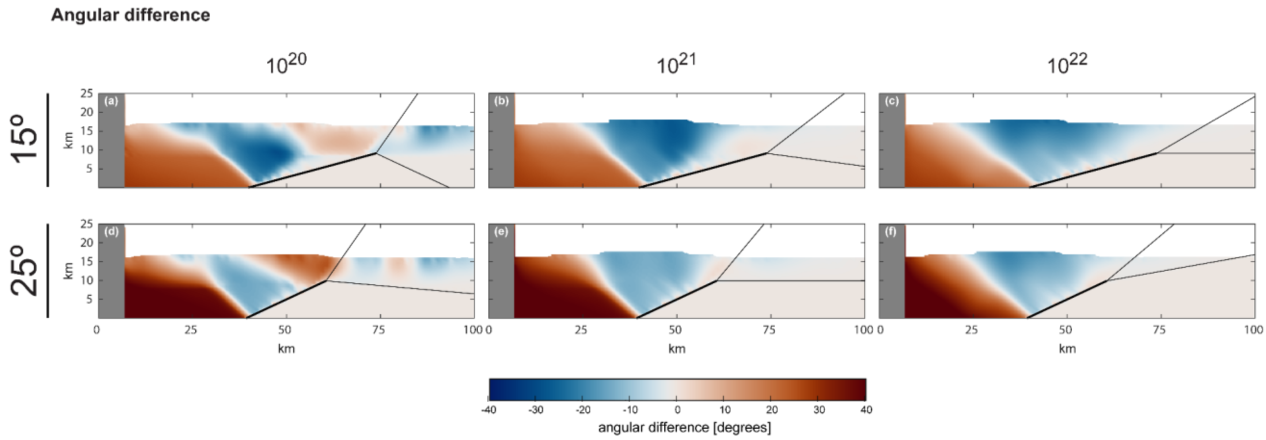

Figure 5: Angular difference between the velocity vectors of the theoretical trishear and the finite element model (trishear - FE). Black fine lines indicate the apical angle applied for the trishear method (table 2). The thick black line is the main reverse fault. Red tones indicate higher angular values in the trishear theoretical model, whereas blue tones represent the opposite.

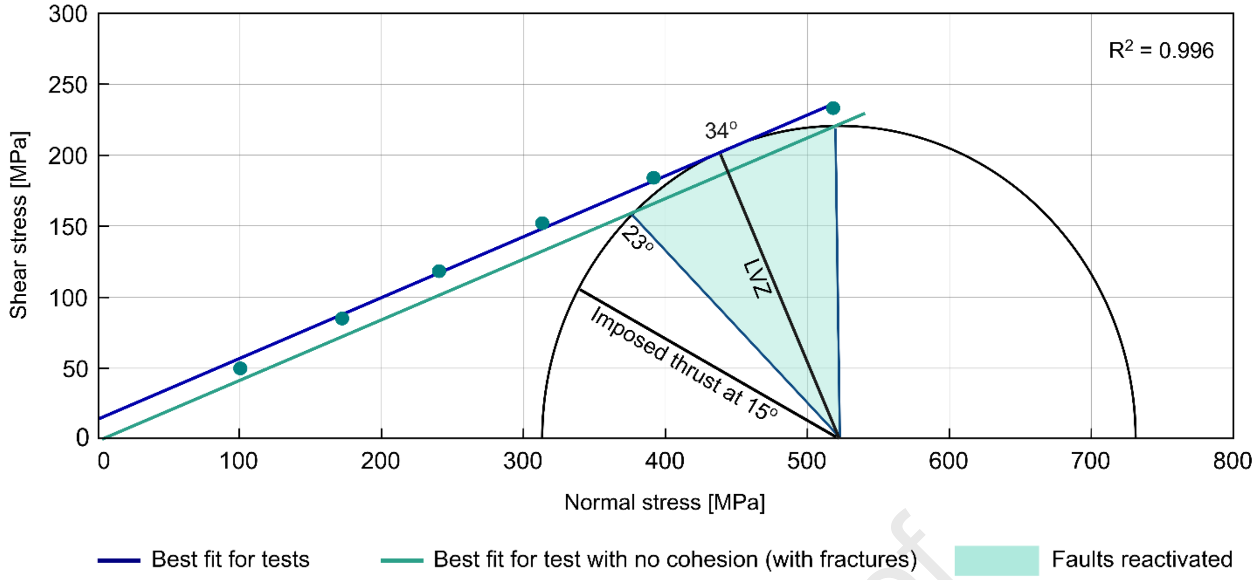

Figure 6: The Mohr-Coulomb circle constructed based on principal stresses obtained from the finite element tests. The green dots represent the results of normal stress and shear stress for each triaxial test. The blue and green lines correspond to the best fit for triaxial tests and tests without cohesion, respectively. The area enclosed by the intersections of the green line and the circle indicates the faulting angle. Faults with angles below 23° will not undergo reactivation. In our FE simulations, with a 15° fault, the main thrust is not reactivated. A new fault (LVZ) is generated following the angle of the envelope for the basement without previous weaknesses (blue line).

Gray versions:

Figure 1

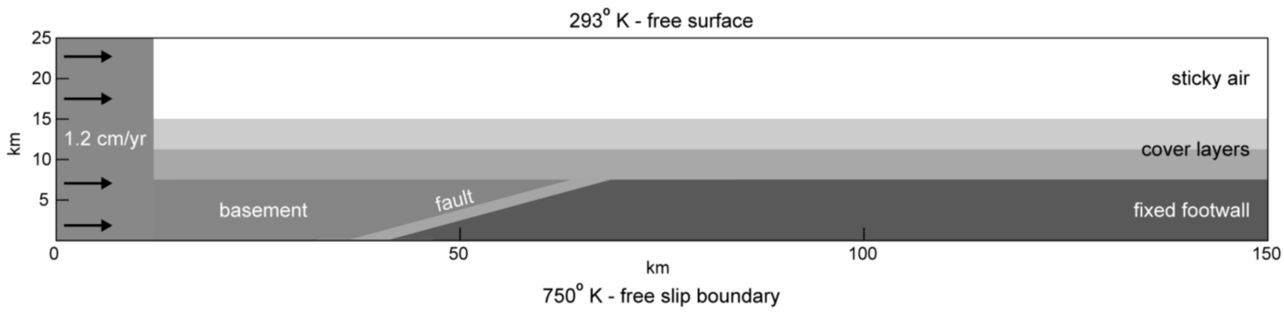

Figure 2

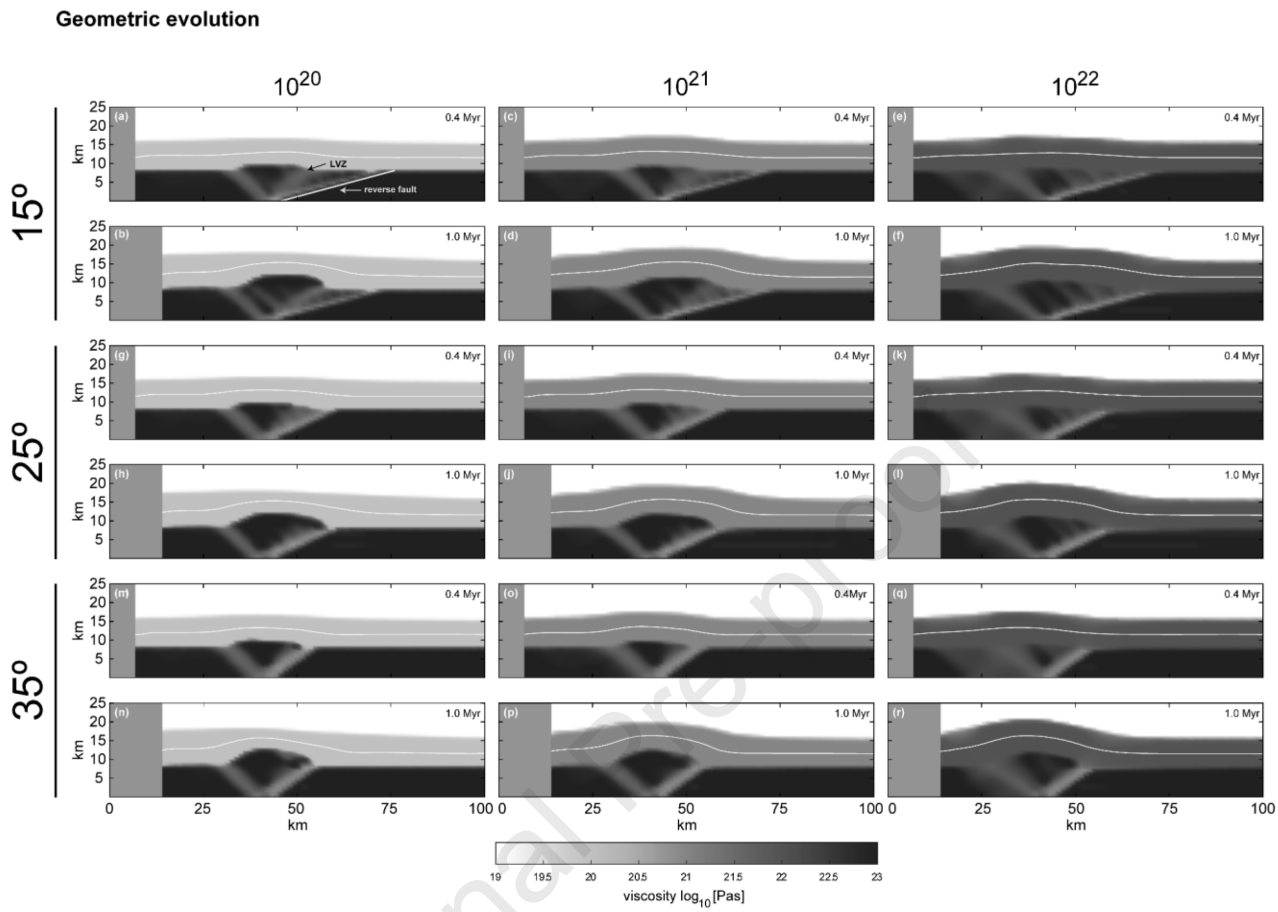
Geometric evolution
10^20
10^21
10^22
15°
25°
35°
(a) 0.4 Myr
(b) 1.0 Myr
(c) 0.4 Myr
(d) 1.0 Myr
(e) 0.4 Myr
(f) 1.0 Myr
(g) 0.4 Myr
(h) 1.0 Myr
(i) 0.4 Myr
(j) 1.0 Myr
(k) 0.4 Myr
(l) 1.0 Myr
(m) 0.4 Myr
(n) 1.0 Myr
(o) 0.4Myr
(p) 1.0 Myr
(q) 0.4 Myr
(r) 1.0 Myr
LVZ
reverse fault
km
viscosity log10 [Pas]

Figure 3

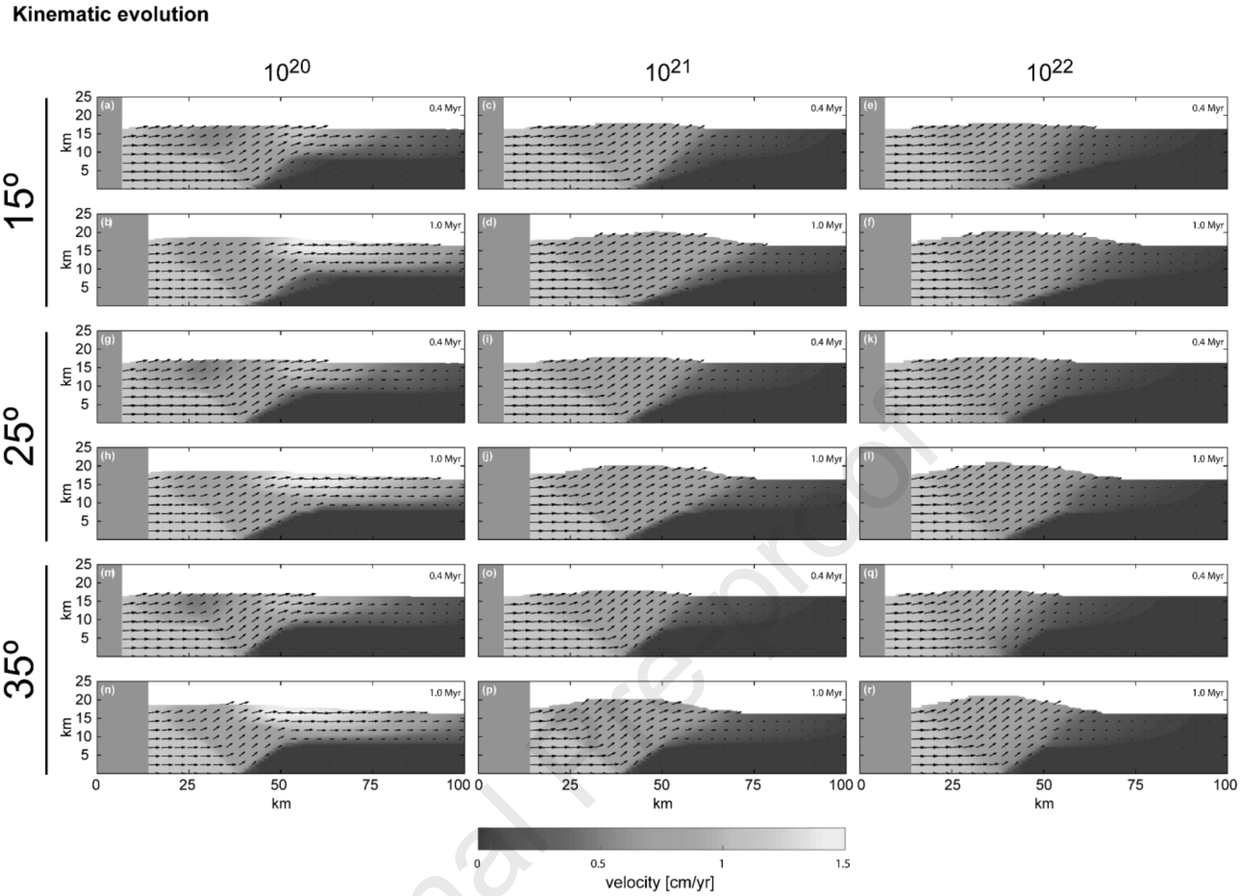
Kinematic evolution
10^20
10^21
10^22
15º
25º
35º
0.4 Myr
1.0 Myr
km
velocity [cm/yr]
0
0.5
1
1.5

Figure 4

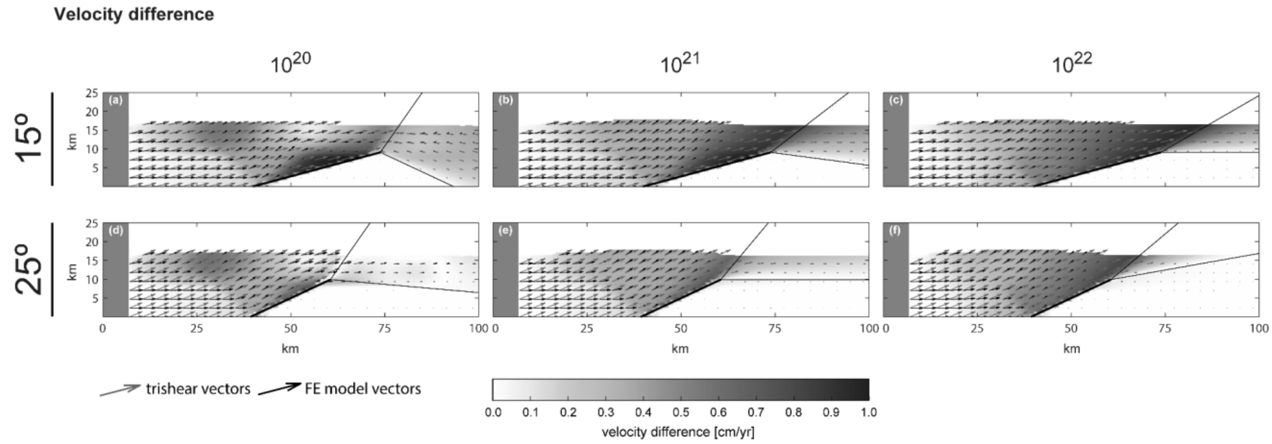
Velocity difference
10^20
10^21
10^22
15º
25º
(a)
(b)
(c)
(d)
(e)
(f)
km
trishear vectors
FE model vectors
velocity difference [cm/yr]

Figure 5

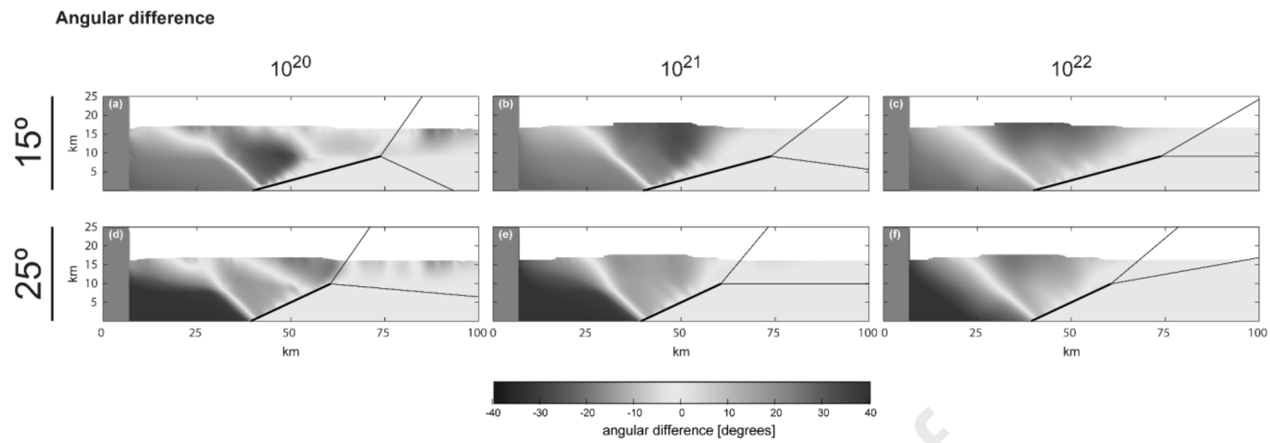

Angular difference
10^20
10^21
10^22
15°
25°
(a)
(b)
(c)
(d)
(e)
(f)
km
0
25
50
75
100
5
10
15
20
-40
-30
-20
-10
0
10
20
30
40
angular difference [degrees]

Figure 6

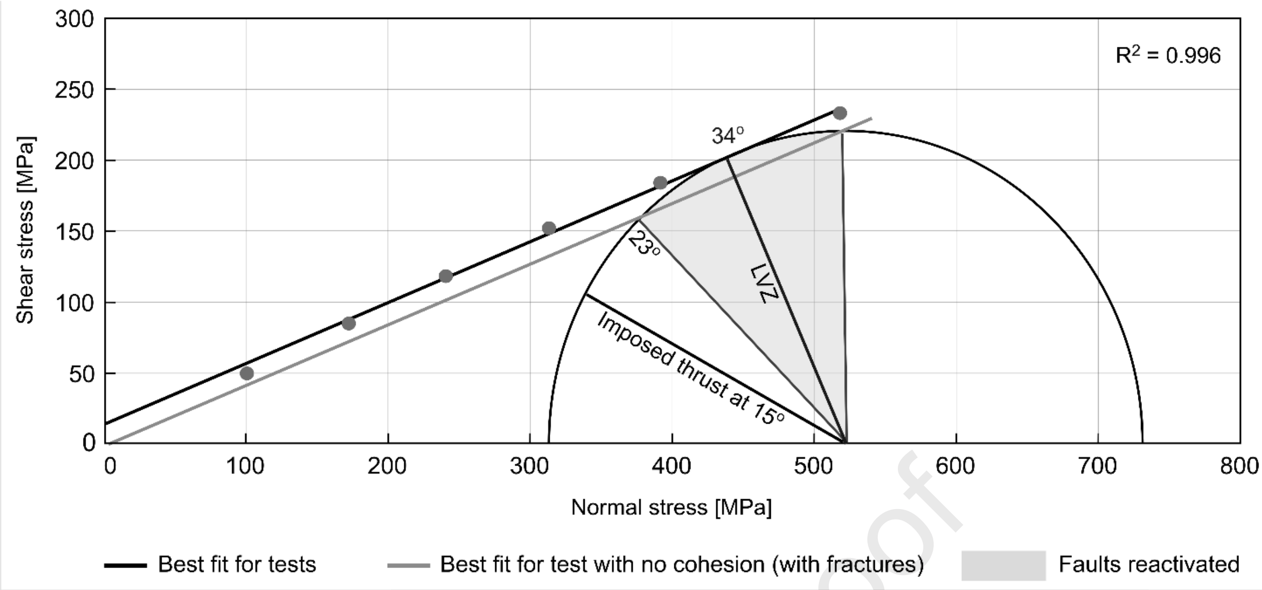
R² = 0.996
34°
23°
LVZ
Imposed thrust at 15°
Shear stress [MPa]
Normal stress [MPa]
0
50
100
150
200
250
300
0
100
200
300
400
500
600
700
800
Best fit for tests
Best fit for test with no cohesion (with fractures)
Faults reactivated

Highlights:

- Fault-propagation folds were investigated using numerical models.
- Kinematic fields were analyzed and compared to the trishear model.
- Increasing viscosity of the layers led to a decrease in the predicted apical angle.
- Simulations with a viscosity of 10^{22} Pa s followed the trishear kinematic pattern.
- The simulations revealed a low viscosity zone when the fault angle was 15°.

Declaration of interests

☒ The authors declare that they have no known competing financial interests or personal relationships that could have appeared to influence the work reported in this paper.

☐ The authors declare the following financial interests/personal relationships which may be considered as potential competing interests: